Nuclear Instruments and Methods in Physics Research A ∎ (∎∎∎∎) ∎∎∎–∎∎∎

Contents lists available at ScienceDirect

Nuclear Instruments and Methods in Physics Research A

journal homepage: www.elsevier.com/locate/nima

Ion acceleration and plasma jet formation in ultra-thin foils undergoing expansion and relativistic transparency

M. King [a], R.J. Gray [a], H.W. Powell [a], D.A. MacLellan [a], B. Gonzalez-Izquierdo [a], L.C. Stockhausen [b], G.S. Hicks [c], N.P. Dover [c], D.R. Rusby [a,d], D.C. Carroll [d], H. Padda [a], R. Torres [b], S. Kar [e], R.J. Clarke [d], I.O. Musgrave [d], Z. Najmudin [c], M. Borghesi [e], D. Neely [d], P. McKenna [a,*]

[a] SUPA Department of Physics, University of Strathclyde, Glasgow G4 0NG, UK
[b] Centro de Laseres Pulsados (CLPU), Parque Cientifico, Calle del Adaja, s/n. 37185 Villamayor, Salamanca, Spain
[c] The John Adams Institute for Accelerator Science, Blackett Laboratory, Imperial College London, London SW7 2BZ, UK
[d] Central Laser Facility, STFC Rutherford Appleton Laboratory, Oxfordshire OX11 0QX, UK
[e] Centre for Plasma Physics, Queens University Belfast, Belfast BT7 1NN, UK

ARTICLE INFO

Keywords:
Laser-driven ion acceleration
Plasma jet
Intense laser–plasma interaction
Relativistic induced transparency

ABSTRACT

At sufficiently high laser intensities, the rapid heating to relativistic velocities and resulting decompression of plasma electrons in an ultra-thin target foil can result in the target becoming relativistically transparent to the laser light during the interaction. Ion acceleration in this regime is strongly affected by the transition from an opaque to a relativistically transparent plasma. By spatially resolving the laser-accelerated proton beam at near-normal laser incidence and at an incidence angle of 30°, we identify characteristic features both experimentally and in particle-in-cell simulations which are consistent with the onset of three distinct ion acceleration mechanisms: sheath acceleration; radiation pressure acceleration; and transparency-enhanced acceleration. The latter mechanism occurs late in the interaction and is mediated by the formation of a plasma jet extending into the expanding ion population. The effect of laser incident angle on the plasma jet is explored.

1. Introduction

Intense laser-driven ion acceleration from thin foils offers a route towards the creation of compact, high energy, short pulse ion sources. These sources could potentially be applied to ion oncology and the fast ignition approach to inertial confinement fusion [1,2]. Over the past 15 years, the target normal sheath acceleration (TNSA) mechanism [3] has been investigated as a promising acceleration mechanism to achieve this end. Whilst much progress has been made, the spectral control and high maximum energies required (particularly for oncology) has not yet been achieved [4,5]. Recent advances in ultra-thin foil targetry and enhancements in laser peak intensity and contrast have led to investigations of new acceleration mechanisms, with promising potential for ion energy scaling and spectral and divergence control.

The irradiation of sub-μm-thick foils with ultra-intense ($>10^{20}$ W cm^{-2}) laser pulses can result in a variety of ion acceleration mechanisms. The TNSA mechanism will typically occur early on the rising edge of the laser pulse as electrons at the target front side are heated and drive the formation of sheath fields. As the laser intensity continues to increase on the rising edge, the radiation pressure acceleration (RPA) mechanism [6], in which the target surface is directly driven forward due to the pressure of the incident laser radiation, can occur. This mechanism is predicted to produce an ion beam with a narrow energy spectrum, low divergence and a favourable energy scaling [7,8]. In the case of ultra-thin (nanometer-scale) foil targets, the RPA mechanism can become unstable to Rayleigh–Taylor-like transverse instabilities, resulting in bubble-like structures in the resulting proton beam [9]. If during the interaction the plasma electron population gets heated and decompressed to the extent that the target undergoes relativistic-induced transparency (RIT) [10], RPA ceases and the remainder of the laser pulse propagates through the target. This gives rise to volumetric heating of the target electrons, which can enhance the energy of the TNSA accelerated ions. This mechanism is referred to as transparency-enhanced acceleration or the break-out afterburner (BOA) scheme

* Corresponding author.
E-mail address: paul.mckenna@strath.ac.uk (P. McKenna).

http://dx.doi.org/10.1016/j.nima.2016.02.032
0168-9002/

[11,12]. The collective plasma electron response to the onset of RIT can give rise to asymmetric electron beam distributions [13] and controllable plasma structures [14]. We have recently shown that in the case of relatively long (hundreds of femtoseconds) laser pulses, the plasma can expand tens of microns during the laser pulse interaction, giving rise to conditions in which a jet of high energy electrons can be produced, driving enhanced laser energy coupling in a localised region of the sheath-accelerated ion population [15].

In this paper, following on from results reported in our earlier paper [15], we report on the influence of the angle of incidence of the laser light on the formation of the plasma jet and the complex dynamics occurring during the onset of RIT.

2. Experiment results

Using the Vulcan petawatt laser at the Rutherford Appleton Laboratory, pulses of 1.054 μm-wavelength light, with (1.0 ± 0.2) ps duration (full width at half maximum, FWHM) and (200 ± 15) J energy were focused onto an aluminium target with a thickness of 10 nm. The spot size was 7.3 μm (FWHM) producing a peak intensity of 2×10^{20} W cm^{-2}. A plasma mirror was employed to improve the laser intensity contrast by a factor of ≈ 100. The angle of incidence of the laser light with respect to the target normal was set at either near-normal (0°) or 30°. In all cases the laser pulse was p-polarised.

The focus of the experimental results presented here is the proton spatial-intensity profile, as measured using a stack of radiochromic (dosimetry) film (RCF). The stack contains filters which enables the energy of the protons stopped at each RCF layer to be set. It was positioned 7.5 cm behind the target with the centre off-set to position the laser axis close to one side as illustrated in Fig. 1. Both the beams of protons accelerated along the laser axis and target normal can be detected on the same RCF stack when the incident angle is changed to 30°. A narrow slot along the central horizontal axis of the stack enabled ion energy spectra measurements using a Thomson parabola spectrometer.

Example measurements of the proton spatial-intensity distribution, obtained with a 10 nm-thick aluminium target irradiated at 0° and 30° incident angle is shown in Fig. 2. The dashed lines are reference circles corresponding to 15° and 30° with respect to the laser propagation axis. From these measurements, it is clearly observed that different proton beam features are separated when the target is irradiated at an oblique angle. Three features are observed, and labelled A–C in Fig. 2 to aid the discussion below.

The annular ring-like distribution (labelled feature A) is consistent with proton spatial profiles previously measured in targets undergoing RIT [12,16]. For this particular target, the ring has a divergence half-angle of $\sim 12°$. From Fig. 2(a), feature A is centred directly along the laser propagation axis for an incidence angle of 0°. The protons present in this feature have been driven by TNSA at the rear of the target. This is demonstrated in Fig. 2(b) when the angle of incidence is changed to 30°. In this case, the annular ring-like structure is still present with a similar divergence half-angle, centred at $\sim 30°$ which is along the target normal axis.

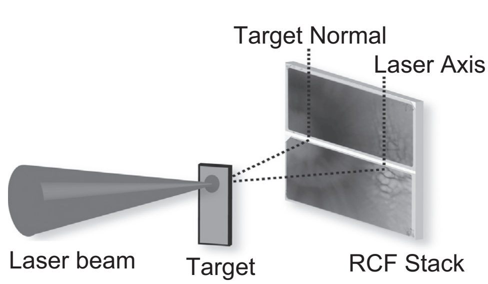

Fig. 1. Schematic illustrating the experimental arrangement.

Feature B comprises small bubble-like structures, similar to that observed due to the transverse instabilities associated with RPA [9]. In Fig. 2(a) these bubble-like structures are contained within a circular area up to $\sim 15°$ around the laser propagation axis. As these are structures associated with RPA in an expanding plasma, they are observed along the laser axis in Fig. 2(b). The bubbles appear elongated along the laser polarisation axis, suggesting an additional effect from interacting at a non-normal incidence.

Feature C is difficult to distinguish at near-normal incidence in Fig. 2(a) as it overlaps with the bubble-like structures. When irradiating at 30° incidence angle, a strong feature can be seen between the target normal and the laser axes. This is associated with the formation of an electron jet from the rear of the target that is created in the expanding plasma as the target undergoes RIT [15]. This jet feature is found to be susceptible to hosing and is observed to vary in position from shot-to-shot. It is thus problematic to measure the ion energy spectrum produced by this feature using a fixed spectrometer sampling a small solid angle. From the RCF data, feature A is only observed up to energies of ~ 15 MeV, whereas feature C is observed up to ~ 26 MeV. The maximum energy of feature B is harder to determine because the bubble-like structure is hard to resolve at higher energies. A fuller discussion of the proton energies, together with spectra, is presented in Ref. [15].

3. Simulation results

To investigate the features observed experimentally, 2D and 3D PIC simulations were undertaken using the EPOCH code [17]. For the 2D simulations, the simulation box was defined as 130 μm × 72 μm, with 26 000 × 7200 mesh cells. The simulations were run with a target thickness of 40 nm due to computational constraints at the resolution required for 10 nm simulations. The main target was initialised with an electron density $n_e = 630 n_c$ (where n_c is the critical density) neutralised with the Al^{11+} ions. A neutral layer of 12 nm H^+ ions with $n_e = 60 n_c$ is initialised on the rear of the target to act as proton source. The initial electron temperature for both the target and the surface layer is set to 10 keV. To simplify the simulation, there is no front surface layer and no carbon or oxygen species present. Simulations are undertaken with the target at both normal incidence to the laser and at a 30° incidence. The incoming laser pulse was linearly polarised along the Y-axis and focused to a transverse Gaussian profile with a FWHM of 5 μm at the front of the target (defined as $X = 0$ μm) with the temporal profile defined as a Gaussian pulse with a FWHM of 570 fs.

In the 3D simulations, the simulation box was defined as 55 μm × 14.4 μm × 14.4 μm with 2000 × 360 × 360 mesh cells. Due to the reduction of mesh resolution the target (Al^{11+}) and contamination layer (H^+) was pre-expanded to a Gaussian spatial profile along the target normal axis with a peak electron density of $n_e = 53 n_c$ and $n_e = 5 n_c$ maintaining the same areal density as the 2D simulation. Simulations were run with the target at both 0° and 30° incidence. The laser pulse temporal duration was slightly reduced to 500 fs and the spatial profile was focused to a 2D Gaussian profile with a FWHM of 5 μm at the front of the target, again linearly polarised along the Y-axis.

Fig. 3 shows example density plots of the electrons (a) and (b) and ions (c) and (d) for simulations at both 0° and 30° incidence angle, 0.3 ps after the peak of the laser pulse has interacted with the target.In both cases the laser pulse enters the system at $X = -30$ μm, with the spatial profile centred at $Y = 0$ μm. As the